On the use of a split Hopkinson pressure bar in structural geology: High strain rate deformation of Seeberger sandstone and Carrara marble under uniaxial compression

Ruprecht Zwiessler [a, *], Thomas Kenkmann [a], Michael H. Poelchau [a], Siegfried Nau [b], Sebastian Hess [b]

[a] Albert-Ludwigs-Universität Freiburg, Institut für Geo- und Umweltnaturwissenschaften, Geologie, 79104 Freiburg, Germany
[b] Fraunhofer Institut für Kurzzeitdynamik (EMI), Eckerstrasse 4, 79104 Freiburg, Germany

ARTICLE INFO

ABSTRACT

There is increasing evidence that seismogenic fractures can propagate faster than the shear wave velocity of the surrounding rocks. Strain rates within the tip region of such super-shear earthquake ruptures can reach deformation conditions similar to impact processes, resulting in rock pulverization. The physical response of brittle rocks at high strain rates changes dramatically with respect to quasi-static conditions. Rocks become stiffer and their strength increases. A measure for the dynamic behavior of a rock and its strain dependency is the dynamic increase factor (*DIF*) which is the ratio of the dynamic compressive strength to the quasi-static uniaxial compressive strength. To investigate deformation in the high strain rate regime experimentally, we introduce the split Hopkinson pressure bar technology to the structural geology community, a method that is frequently used by rock and impact engineers. We measure the stress-strain response of homogeneous, fine-grained Seeberger sandstone and Carrara marble in uniaxial compression at strain rates ranging from 10^{+1} to 10^{+2} s^{-1} with respect to tangent modulus and dynamic uniaxial compressive strength. We present full stress-strain response curves of Seeberger sandstone and Carrara marble at high strain rates and an evaluation method to determine representative rates of deformation. Results indicate a rate-dependent elastic behavior of Carrara marble where an average increase of ~18% could be observed at high strain rates of about 100 s^{-1}. *DIF* reaches a factor of 2.2—2.4. Seeberger sandstone does not have a rate-dependent linear stress-strain response at high strain rates. Its *DIF* was found to be about 1.6—1.7 at rates of 100 s^{-1}. The onset of dynamic behavior is accompanied with changes in the fracture pattern from single to multiple fractures to pervasive pulverization for increasing rates of deformation. Seismogenic shear zones and their associated fragment-size spectra should be carefully revisited in the light of dynamic deformation.

1. Introduction

Rocks can be exposed to high loading rates and fast strain rates by a number of sudden geo-hazards such as meteorite impact, earthquake faulting, explosive volcanism, gravitational mass movements, and lightening strike. The final product of such events are strongly fractured, brecciated and even pulverized rocks (Davies and McSaveney, 2009; Kenkmann et al., 2014; Fondriest et al., 2015). Heating by friction or adiabatic pressure release can even melt these rocks (e.g., Spray, 2010; Di Toro et al., 2011). High rates of loading induce changes in the mechanical properties and the fracture behavior (e.g., Ramesh et al., 2015) that may strongly deviate from behaviors for quasi-static conditions. Deformation behavior and rock failure for quasi-static conditions including fracture initiation and propagation are rather well understood (e.g., Zang et al., 2000; Scholz, 2002). Brittle deformation under quasi-static conditions is insensitive to the loading rate, but responds sensitively to confinement and pore pressure.

The critical strain rate above which a rate dependency on strength occurs in rocks varies between 10^{+0} and 10^{+2} s^{-1} (Zhang

and Zhao, 2014) and represents the onset of the so-called high strain rate regime (HSR) (Zhang and Zhao, 2014). Obviously, deformation during hypervelocity meteorite impact events occurs in the high strain rate regime, for positions close to the point of impact (Melosh, 1989; Kenkmann et al., 2014). However, evidence is increasing that seismogenic fractures propagate fast and likely deform rocks in the high strain rate regime. The majority of earthquake ruptures tend to propagate with an average velocity that is about 80% of the shear wave velocity (Heaton, 1990). Yet, super-shear earthquake ruptures even propagate faster than the shear wave velocity (Passelèque et al., 2013) of the surrounding rocks. Strain rates within the tip region of such super-shear ruptures are comparable to deformation conditions that develop during impact processes. For instance, the 2001 Kunlunshan earthquake produced a 400-km-long surface rupture. Bouchon and Vallée (2003) determined that the rupture propagated at an average speed of 3.7–3.9 km/s, which exceeds the shear velocity of the brittle part of the crust. Mode II fracturing started at sub-–Rayleigh wave velocity and became super-shear, probably approaching 5 km/s, after about 100 km of propagation.

Super-shear rupture events during earthquakes can produce pervasively pulverized rocks up to several hundred meters from the fault core, indicating high strain rates. Doan and Gary (2009) reported such intensively fragmented fault rocks up to 400 m from the fault core at San Andreas Fault, exhibiting textures of low total strain. Similar observations by Fondriest et al. (2015) found highly shattered to pulverized dolostones within the exhumed seismogenic Foiana Fault zone in the Southern Italian Alps, generated in absence of significant shear strain.

Using the split Hopkinson pressure bar (SHPB) technique for testing intact samples, Doan and Gary (2009) showed that high strain rates are necessary to reproduce the fracture pattern of these natural examples and experiments showed a related increase of rock strength at dynamic conditions. Similarly, Yuan et al. (2011) experimented on Westerly granite to ascertain the critical-stress wave loading conditions required for the change in fracturing behavior from discrete fracturing to pervasive pulverization. Reches and Dewers (2005) compared examples of pulverized rocks of fault gouges from different settings according to their grain size distribution. They attributed the formation of these gouges to fast-propagating earthquake ruptures and calculated models for the surrounding rock deformation history of a dynamic shear fracture propagating at speeds close to the Rayleigh wave velocity. They concluded that for strain rates of up to 10^{+5} s^{-1}, occurring close to the fracture tip, extreme rates of subsequent volumetric expansion and contraction produced the pervasively pulverized fault rocks. To summarize, slip rates and the crack propagation along tectonic shear zones can reach conditions during displacement where the dynamic mechanical behavior becomes important. Knowledge about the changing properties of rocks at high strain rates obtained by SHPB methodology is required and can provide new insights into the propagation of faults and earthquakes. This can significantly improve our understanding of the deformation inventory of faults in the field, and is the focus of the contribution of this paper.

Meteorite impacts are the natural processes with the greatest loading and strain rates. Depending on the kinetic energy of the impacting body, initial shock pressures are in the order of several hundred GPa, and strain rates reach 10^{+6} - 10^{+8} s^{-1} (e.g., Melosh, 1989). However, by geometric thinning and attenuation due to irreversible deformation, phase transformations, and heating, shock waves transform into elastic pressure waves. Consequently, wide spectra of pressure, strain, and strain rate are realized within a single impact event (O'Keefe and Ahrens, 1975; Collins et al., 2005; Kenkmann et al., 2014). Buhl et al. (2013) showed that the strain rate in experimentally produced impact craters decays strongly

with time and with distance from the impact point. The decrease in strain rate could be correlated with a change from pervasive grain pulverization with a power law exponent >2.4 of the particle size distribution to discrete fracturing with power law exponents distinctly below 2. The great fracture densities at high strain rates and low bulk strain were explained by the activation of abundant micro-flaws simultaneously with abundant crack branching. To understand the fragmentation behavior of rocks in the high strain rate regime, the dynamic strength properties of rocks in this regime have to be measured, and we will do so, utilizing SHPB methods (Millon et al., 2016; Ramesh et al., 2015).

Rocks deformed in the high strain rate regime are sensitive to strain rate in terms of their stress-strain response as well as in their mode of failure and strength during both compression and tension. In general, increasing tangent moduli and either increasing or decreasing critical strain have been observed for a diversity of rocks (Zhang and Zhao, 2014, and references therein). Failure mechanisms change from single to multiple fracturing, and ultimately lead to rock pulverization accompanied by increasing energy absorbance, as shown experimentally by Hakalehto (1970), Li et al. (1993) and Hong et al. (2009). More inherent flaws are activated at high strain rates to accommodate strain (Grady and Kipp, 1993).

Kimberley et al. (2013) presented scaling laws for the rate dependent strength in uni-axial compressive and tensile regimes in brittle materials. These scaling laws correlate the pre-existing flaw densities and their size and spacing to the changing fracture pattern and energy degradation during failure. The propagation speed of mechanical information, given by the P-wave velocity and the limited propagation velocity of wing cracks (typically a fraction of the Rayleigh wave speed) represent key factors of the dynamic behavior. At high loading rates beyond a critical material-dependent threshold, the weakest flaws are not capable of causing macroscopic failure before other, increasingly stronger flaws are activated. Hence, according to the statistical theory of Hild et al. (2003), the onset of multiple fracturing is linked to an intrinsic increase in material strength, since more energy is required for the propagation of numerous fractures. Furthermore, properties like pore space, fluids, grain-size distribution, presence of twin lamellae and the interplay of different mineral phases influence the bulk dynamic behavior of rocks.

The current study is aimed at comparing the dynamic behavior of sandstone and marble, while familiarizing the structural geology community with the SHPB technology, a powerful technique of dynamic mechanical testing. We deliberately selected this journal for publication of this work because we are convinced that rate-dependent brittle deformation is of great importance for understanding the deformation inventory of seismogenic shear zones in the field. The time is ripe to bridge the gap between impact engineering and rock dynamics on the one side and structural geology on the other side.

2. Methodology of the split Hopkinson pressure bar technique: setup and theory

The experiments were performed with a 5 cm diameter split Hopkinson pressure bar (SHPB), characterizing the dynamic response of Seeberger sandstone and Carrara marble at dynamic conditions. The loading technique represents a precise tool that enables the experimentalist to induce diverse stress histories in cylindrical samples. The experiments cause one-dimensional states of stress for controlled conditions including longitudinal stress equilibrium and constant strain rates. Additionally, a uniaxial loading frame was used to obtain reference values of compressive strength and the Young's modulus at quasi-static conditions.

2.1. Lithologies used for the experiments

The current study compares two lithologies for their mechanical behavior during uniaxial compression. Seeberger sandstone is a fine grained (76—125 μm grain size), well sorted and porous fluvial sediment of upper Triassic (Rhätian) age, deposited within the Thuringian basin in Germany. It mainly consists of sub-rounded quartz grains with thin coatings of iron oxides and clay minerals and is weakly bonded by silicate cementation. It has prominent Liesegang bands of finely dispersed iron oxides. Feldspar, mica, zircon and hematite are present as accessory minerals. It is quarried by TRACO Company at Seeberg near Gotha, Germany from a specific stratigraphic layer 3 (Ebert et al., 2013).

Carrara marble is quarried by the Amso International Company in northern Tuscany, Italy, and belongs to the middle Liassic carbonate platform of the former Italo-Adriatic continental margin and experienced a greenschist facies metamorphism during the Apennine orogeny. According to Pieri et al. (2001) it contains 98% Calcite, occasionally quartz, mica, dolomite, epidote and pyrite. Light gray trails of very fine grained phyllosilicates are typical. Chemical and physical properties of both lithologies are given in Table 1.

2.1.1. Sample preparation

We used oven dried cylindrical samples of 4 cm length and 4 cm diameter for the analysis with the SHPB-technique. Seeberger sandstone samples were cored perpendicular to the sedimentary layering so the pronounced Liesegang bands strike across samples at different angles (Fig. 1). Carrara marble appears macroscopically isotropic with randomly distributed spots that contain small amounts of phyllosilicates and appear darker than most of the material.

Sample dimensions were chosen according to Gray (2000) to minimize end friction and inertia effects while keeping the sample size as large as possible. Although a sample length to diameter ratio of 2 represents a standard in conventional uniaxial compression testing, split Hopkinson bar tests generally are performed on comparably short specimen, such as the length to diameter ratio of 1:1 in the current study to keep the stress equilibrium time short. Both sample facets are polished planes with a maximum misfit of 20 μm in length and lubricated by highly viscous silicone grease to ensure a homogeneous one-dimensional state of stress. Experimental fracture patterns that form of primary orientations parallel to the sample's longitudinal direction indicate a sufficient lubrication, so that end friction effects can be neglected from the analysis. Pulse-shaping techniques were used to minimize dispersion effects, achieve diverse strain rates and stress equilibrium conditions.

Table 1
Composition and physical properties of investigated lithologies.

	Seeberger sandstone	Carrara marble
composition [wt%]	[a]94.77 SiO_2; 3.11 Al_2O_3; 0.45 Fe_2O_3	[c]55.11 CaO; 42.83 Pf; <1(MgO + SiO_2+Al_2O_3)
density [g cm^{-3}]	[b]2.05	[d]2.7
porosity [%]	[b]23.1 ± 4.0	[d]<1
grain size [μm]	[a]76-125	[c]150 average
static strength σ_{ucs} [MPa]	60.4 ± 4.6	88.8 ± 5.7
Young's modulus [GPa]	14.9 ± 1.5	41.1 ± 4.0

Source.
[a] (Ebert et al., 2013).
[b] (Poelchau et al., 2013).
[c] (Pieri et al., 2001).
[d] (Poelchau et al., 2015).

2.2. Setup

For a general introduction to various experimental techniques for dynamic testing, among them the split Hopkinson pressure bar technique, we refer readers to Chen and Song (2010) as well as to Zhang and Zhao (2014). The split Hopkinson pressure bar configuration used for experiments (Fig. 2) consists of an air driven accelerator, bringing strikers of diverse shapes and lengths to speeds of up to 40 m/s, measured by a laser barrier. A planar impact on the 5 cm diameter incident bar generates an acoustic compressive pulse of twice the striker length where striker and bars are made of equal materials, which propagates through the 2.5 m long incident bar. Eventually the pulse encounters the incident bar/sample interface. The longitudinal speed of sound in the bar material C_B, given by Eq. (1) depends on its Young's modulus E_B and density ρ.

$$C_B = \sqrt{\frac{E_B}{\rho}} \tag{1}$$

In this study, we used a titanium alloy E_B = 110 GPa and ρ = 4.43 g/cm^3, resulting in a wave velocity C_B of approximately 4.98 km/s. A variety of normalized incident pulses can be achieved by the use of conventional cylindrical strikers of different lengths and three pulse shaping techniques, which are used to improve stress equilibrium and to achieve constant strain rates during loading (Fig. 3). We used truncated cone strikers as described in Christensen et al. (1972). Solid aluminum and aluminum foam were used as materials for the pulse shaper discs placed between the striker and incident bar (e.g. Frew et al., 2002). The respective pulse amplitudes in general depend on the speed of the striker, which can be adjusted by the vessel pressure. According to the sample's stress-strain response at the applied strain rate, the incident wave converts into reflected and transmitted portions. Consequently, three strain pulse histories $\varepsilon_I(t)$, $\varepsilon_R(t)$, $\varepsilon_T(t)$, with subscripts I, R and T for incident, reflected and transmitted wave are measured on the bars as a function of time t by strain gauges via Wheatstone quarter bridges at a high temporal resolution of up to 10 MHz. Their evaluation leads to consideration of sample histories in terms of strain rate $\dot{\varepsilon}(t)$, strain $\varepsilon(t)$ and stress $\sigma(t)$.

2.3. SHPB evaluation

2.3.1. Dispersion effects

In SHPB experiments, dispersion effects require consideration, since longitudinal waves in rods with large diameters and large Poisson's ratios undergo changes in their strain pulse history as they travel a certain distance. The measured strain history at the strain gauges is slightly different from the strain history of the bar-to-sample interface. These modifications due to the frequency-dependent speed of sound of all harmonic sinusoidal wave components, are predictable and corrected to gain the real pulse histories of the bars at the samples' interfaces (e.g. Schuler, 2004). Additionally, the time delay is corrected by the time difference $\delta t = \frac{x_{I,T}}{C_B}$, according to the respective strain gauges' distance to the sample $x_{I,T}$ and the longitudinal speed of sound C_B, given by Eq. (1). Experiments performed on our SHPB-device have shown that the use of the dispersion correction and time shifting procedure represents a good alternative to the conventional foot shifting method as described e.g. by Mohr et al. (2010). Arrival times and strain histories of pulses that have propagated several meters through the incident bar, including multiple reflections, were precisely predicted by this method.
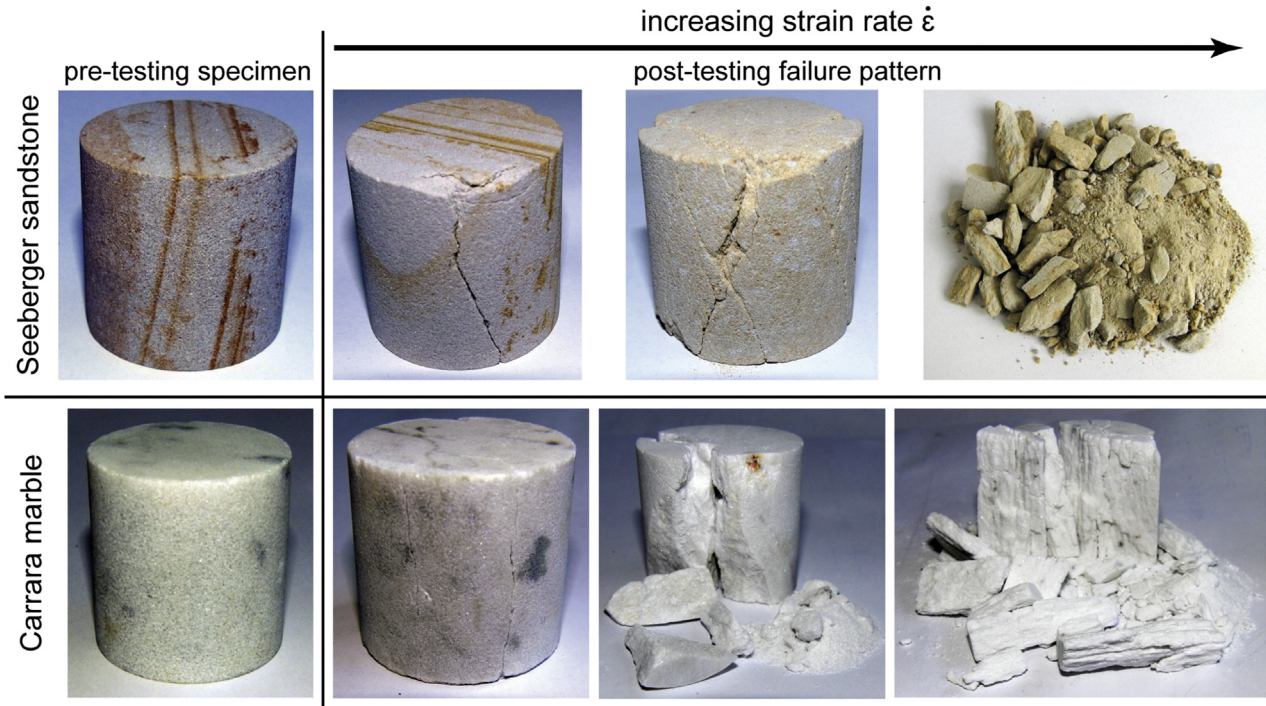
Fig. 1. Samples of Seeberger sandstone and Carrara marble before and after testing for different strain rates. The observed fracture mechanism changes with strain rate from single- to multiple fracturing. Sample dimensions are 4 cm in length and diameter.
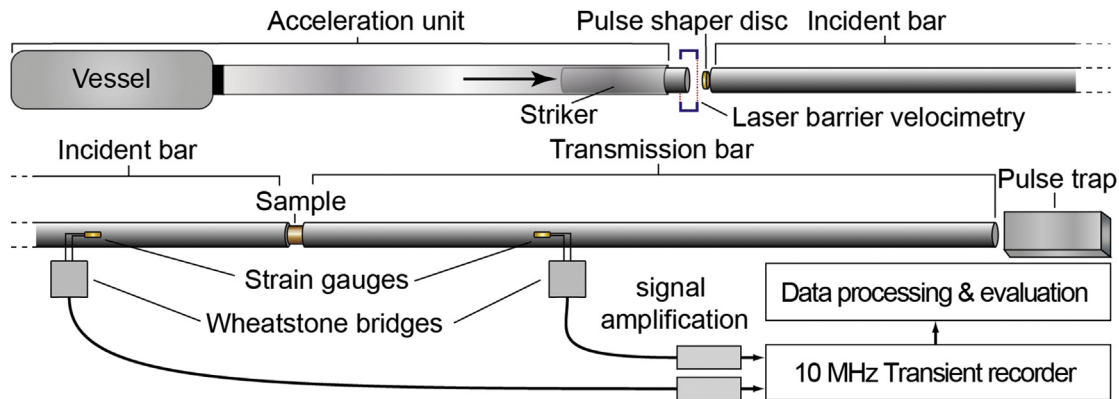
Fig. 2. Schematic illustration of the split Hopkinson pressure bar setup.

2.3.2. Stress equilibrium

From the time corrected pulses, the longitudinal stress histories of both sample facets $\sigma_a(t)$ and $\sigma_b(t)$ (see Fig. 4) are given by Eqs. (2) and (3) (Chen and Song, 2010),

$$\sigma_a(t) = \frac{A_B}{A_S} E_B (\varepsilon_I(t) + \varepsilon_R(t)) \tag{2}$$

$$\sigma_b(t) = \frac{A_B}{A_S} E_B \varepsilon_T(t) \tag{3}$$

with A_B and A_S representing the cross-sectional areas of the bars and sample. Additionally, their mean value calculated by Eq. (4), where

$$\sigma(t) = \frac{A_B E_B}{2 A_S} (\varepsilon_I(t) + \varepsilon_R(t) + \varepsilon_T(t)) \tag{4}$$

is assigned as the actual sample stress according to the three-waves analysis method (Gray, 2000). Since loading rates may exceed a required equilibration time, defined by the sample's length and longitudinal speed of sound, both sample stresses are monitored to assess the requirement of stress equilibrium for valid results. Stress equilibrium is satisfied if the stress gradient in longitudinal sample direction is within 5% of the mean stress, calculated by the percentage ratio of stress difference over time $R(t)$, given by: $R(t) = 200 \left| \frac{\sigma_a - \sigma_b}{\sigma} \right|$ (Ravichandran and Subhash, 1994).

2.3.3. Determination of strain and representative strain rate

Assuming stress equilibrium, the sample's history of strain rate $\dot{\varepsilon}(t)$ and strain $\varepsilon(t)$ are calculated according to the three-waves
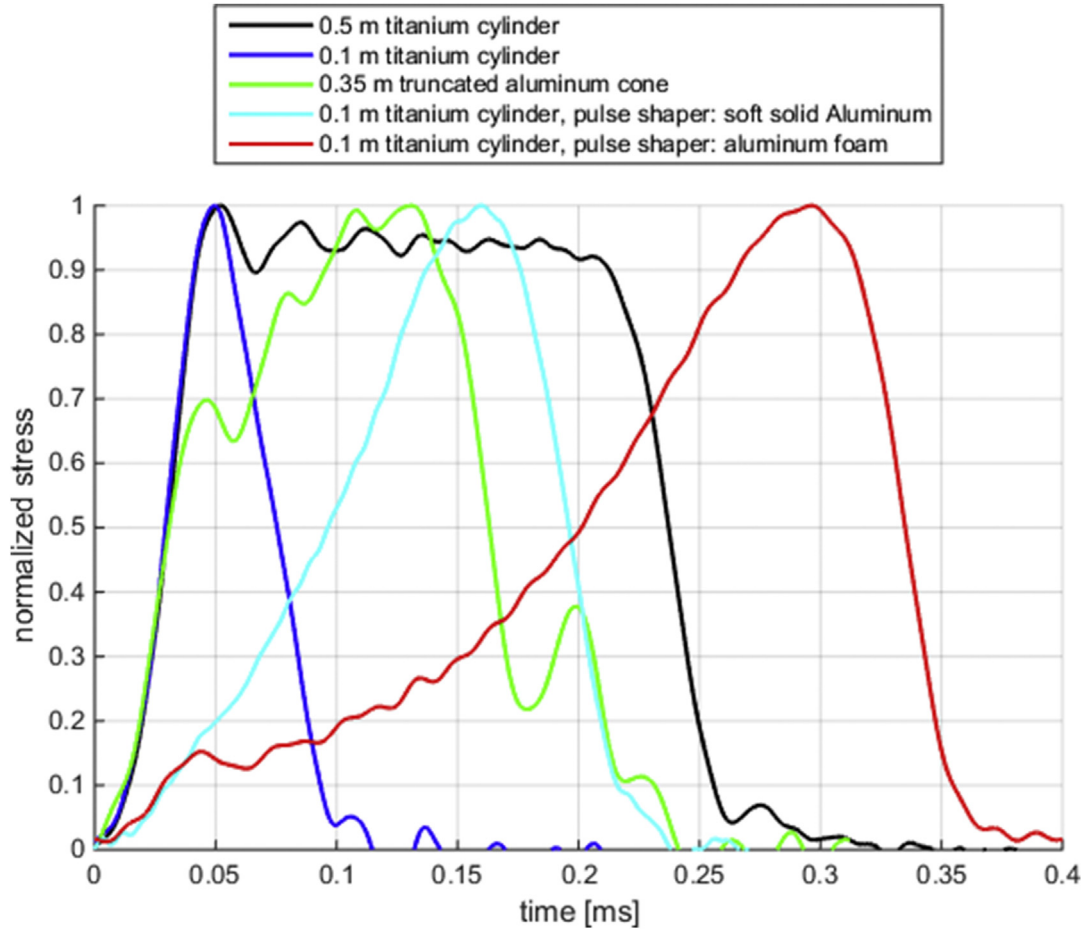
Fig. 3. Normalized incident stress pulses, produced by cylindrical titanium strikers of 0.5 and 0.1 m in length, and modified pulses, generated by a truncated cone striker and pre-stressed aluminum foam as well as solid aluminum as pulse shaper-disc materials between striker and incident bar. The pulses are measured by strain gauges positioned at the longitudinal center of the incident bar. Amplitudes in general depend on the striker speed and pulse histories are subject to dispersion, causing alteration and high frequency oscillations.
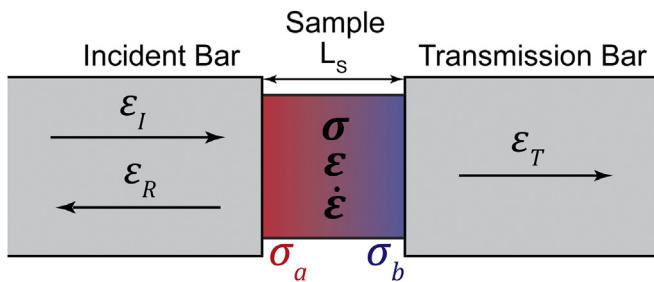
Fig. 4. Incident, reflected and transmitted strain pulse histories are used to determine the stress-, strain- and strain rate histories of the sample. Stress equilibrium is monitored by comparison of both sample facet stresses σ_a and σ_b.

evaluation method by Eqs. (5) and (6).

$$\dot{\varepsilon}(t) = \frac{C_B}{L_S}(\varepsilon_I(t) - \varepsilon_R(t) - \varepsilon_T(t)) \qquad (5)$$

$$\varepsilon(t) = \frac{C_B}{L_S} \int_0^t (\varepsilon_I(t) - \varepsilon_R(t) - \varepsilon_T(t))dt \qquad (6)$$

The second requirement for correct interpretations of SHPB testing results, beside stress equilibrium, is a constant strain rate over time, characterized by a strain plateau in the reflected wave over the full testing duration. The use of various pulse-shaping techniques allows these conditions to be approximated, at least for a certain period of the loading history, but fluctuations are quite common. For instance, due to the reduction of the stress-strain response beyond the yield point and during sample failure, progressive increases of the deformation rate can be expected at constant loading rates. Additionally, so called Pochhammer-Chree oscillations (Chen and Song, 2010), which are generated by dispersion are common in the incident pulse amplitude, cause sinusoidal variations in the strain rate history. Therefore, the determination of the representative strain rate is not trivial in such cases, since strain acceleration (change of strain rate over time) may cause inertia-induced radial confinement on the specimen, increasing its apparent stress resistance additionally to the actual rate dependent enhancement. This effect has a linear relation of mean strain rate and the strain rate at the point of failure (Zhang et al., 2009). Strain rate prior to failure (elastic deformation stage) is assumed to be irrelevant for brittle failure, so they defined the rate of deformation at the point of failure to be the representative strain rate. This assumption neglects the general concept about the dynamically increasing stress resistance due to the prevention of weakest-link coalescence during loading beyond a critical rate of deformation. As described by Kimberley et al. (2013), the limited crack propagation speed may be outpaced by the strain rate, preventing macroscopic failure due to

coalescence of the most prominent flaws at HSR. Therefore, the experimental phase prior to failure significantly contributes to the dynamic effects, during when wing cracks start to grow at greater than the quasi-static yield stress. The incremental strain rate at the point of failure is mainly a function of the applied incident pulse, since its total energy will be reflected once the sample provides no more resistance, producing a high amplitude in the reflected wave, which determines the strain rate.

In the current work, we therefore propose the definition of two representative strain rates: (i) The mean strain rate during linear elastic response $\dot{\varepsilon}_E$ (Fig. 5a) determined across the time span from t_1 to t_2 in the strain rate history (Fig. 5b) was used to analyze the rate dependency of the tangent modulus; (ii) a second representative strain rate $\dot{\varepsilon}_F$ is defined as the mean strain rate from the beginning of the linear elastic response until sample failure from time t_1 to t_3 (Fig. 5) to investigate the dynamic uni-axial compressive strength of the sample. Furthermore, in the stress-strain response curves, both sample stresses σ_a and σ_b are displayed additionally to the three-waves-evaluated sample stress (Eq. (4)) to monitor stress equilibrium and therefore data validity. The respective slope of the apparent linear section in the stress-strain curve represents the dynamic tangent modulus of the sample and has been investigated by fitting linear equations to the three-waves-evaluated stress and strain, using the least squares method.

The Seeberger sandstone specimen has been deformed by a relatively short incident pulse of high average amplitude, containing pronounced high frequency oscillations which caused similar oscillations in the strain rate history (Fig. 5b). As a consequence, sample stress histories are in permanent disequilibrium, and therefore, the determined tangent modulus of 12.7 GPa represents an estimate only (Fig. 5a). The Carrara marble specimen was loaded with a longer incident pulse of relatively low amplitude, causing a lesser average strain rate. Due to the absence of strong oscillations, a higher grade of stress equilibrium is reached, where stress-strain response curves of all evaluation methods follow a single curve (Fig. 5a). Its tangent modulus can be estimated more precisely at about 40 GPa, although the strain rate varies over a longer period, too.

3. Results

We conducted numerous experiments on Seeberger sandstone and Carrara marble in uniaxial compression at quasi static- and high strain rates (HSR) to investigate their strain rate-dependent tangent modulus and rock strength (Table 2). Nine HSR-tests were performed on the sandstone and 10 on the marble (Fig. 6). Not all samples broke during the initial loading period. Nevertheless, data from experiments with unbroken specimens were investigated for their respective tangent modulus, providing useful information about the resistance against the maximum applied stress at a given strain rate. Some of their resulting stress-strain response curves are represented as well (Fig. 6). Note that it cannot directly be seen from the curves which samples failed and which did not.

Since a pre-loading phase is absent, unlike other uniaxial compression experiments, stress-strain curves obtained with the SHPB are characterized by a large variation in the initial onset of the stress-strain slope independent of the deformation rate. Hence, curves were normalized (shifted along the horizontal strain axis) to the approximate beginning of the linear stress-strain response with 10 MPa for Seeberger sandstone and 20 MPa for Carrara marble, which also implies that the total strain on average was about 1 mm/m greater than illustrated (Fig. 6). Furthermore, for experiments with unsatisfactory stress equilibrium, both sample stresses σ_a and σ_b as defined in Eqs. (2) and (3) are shown as dashed lines. The represented standard deviations of the given strain rates give hints to the rate spectrum and the maximum achieved strain rate during single tests. Stress-strain response curves show the increase of rock strength for dynamic conditions with both rock types. The tangent modulus is unaffected for Seeberger sandstone at the applied strain rates but shows an increase for Carrara marble. In comparison to the quasi-static data, characterized by deformation rates at an order of magnitude of 10^{-5} s^{-1}, the sandstone reveals a greater apparent linear stress-strain response for larger stresses and strains, along equal paths at high strain rates. In contrast, Carrara marble reveals steeper curve slopes for increasing maximum stress and strain. Furthermore, its tangent modulus and maximum strain display a more pronounced scattering.

The relationship of respective deformation rates $\dot{\varepsilon}_E$ and tangent moduli (Fig. 7) at quasi-static and dynamic conditions reveals typical scattering of the apparent elastic response of both natural materials. Note that quasi-static values represent Young's moduli of the material, measured during a second loading cycle after pre-loading of the sample (Jaeger et al., 2009), whereas HSR results represent the stress-strain slope of the initial loading period. In general, the Young's modulus of geomaterials can be expected to be
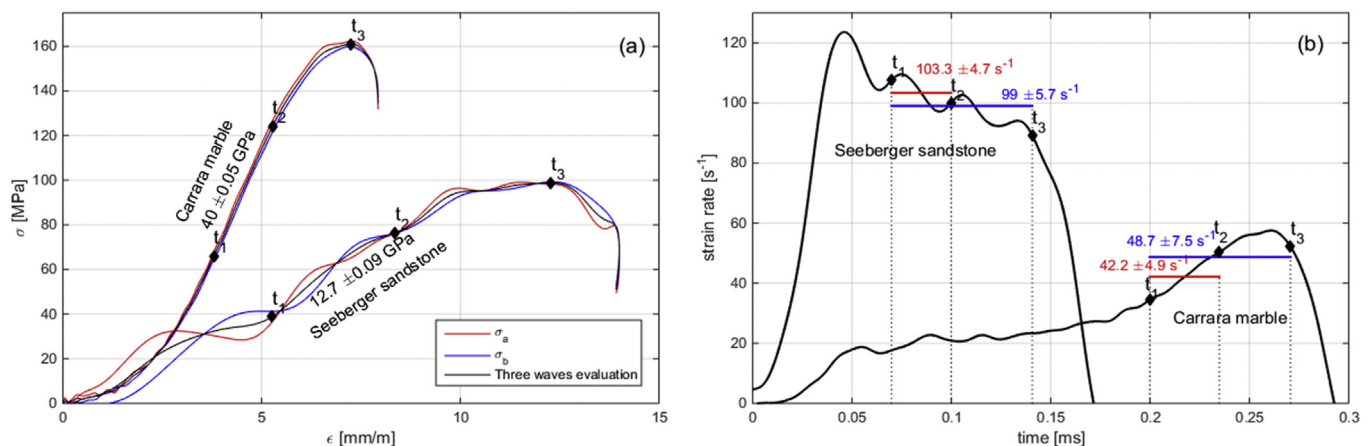
Fig. 5. (a) Axial stress-strain response curves are used to determine the time span of linear elastic response from t_1 to t_2 with associated tangent modulus, which is about 40 GPa for the marble and 12.7 GPa for the sandstone. A second, extended time span from t_1 to the point of failure t_3 is also defined to calculate the representative deformation rate during uniaxial compression. (b) Mean values and standard deviations of representative strain rates are determined from the strain rate histories. Strikers and pulse shaping techniques were used to deform the samples to low maximum strains only, avoiding additional strain after sample failure. Therefore, high strain rate-inducing pulses are characterized by much shorter durations in the strain rate history.

Table 2
Experimental conditions and results of dynamic experiments in uniaxial compression.

	$\dot{\varepsilon}_E$ [s^{-1}]	E_d [GPa]	$\dot{\varepsilon}_F$ [s^{-1}]	σ_{ucd} [MPa]
Seeberger sandstone	21.3 ± 1.1	11.7 ± 0.035	18 ± 5.2	51.01
	16.3 ± 4.5	13.3 ± 0.022	16.36 ± 4.45	51.98
	31.1 ± 6.3	12 ± 0.019	31.06 ± 6.33	63.74
	37.3 ± 9.3	13.4 ± 0.017	37.27 ± 9.30	72.45
	84 ± 12	14.6 ± 0.093	78.94 ± 16.44	91.06
	51.9 ± 1.3	14.5 ± 0.023	47.09 ± 8.02	85.74
	103.3 ± 4.7	12.7 ± 0.095	99.01 ± 5.68	98.73
	86.7 ± 30.3	10.2 ± 0.108	96.48 ± 20.94	101.62
	97.6 ± 8.9	12.6 ± 0.122	89.84 ± 10.82	101.55
Carrara marble	12.84 ± 0.51	49.42 ± 0.111	10.75 ± 3.25	94.18
	23 ± 1.58	40.73 ± 0.045	21.80 ± 2.92	123.9
	33.2 ± 3.01	43.34 ± 0.288	33.37 ± 3.5	147.5
	123.81 ± 18.28	55.48 ± 0.033	129.23 ± 16.28	182.61
	53.88 ± 8.8	41.30 ± 0.12	44.6 ± 10.67	147.22
	43.35 ± 4.42	39.06 ± 0.06	49.77 ± 6.77	161.07
	51.16 ± 2.08	42.10 ± 0.025	58.84 ± 8.11	172.73
	51.67 ± 9.73	60.57 ± 0.112	84.74 ± 42.65	211.71
	49.89 ± 12.64	48.71 ± 0.071	70.7 ± 29.27	197.22
	90.56 ± 14.98	39.46 ± 0.073	117.02 ± 27.87	194.96
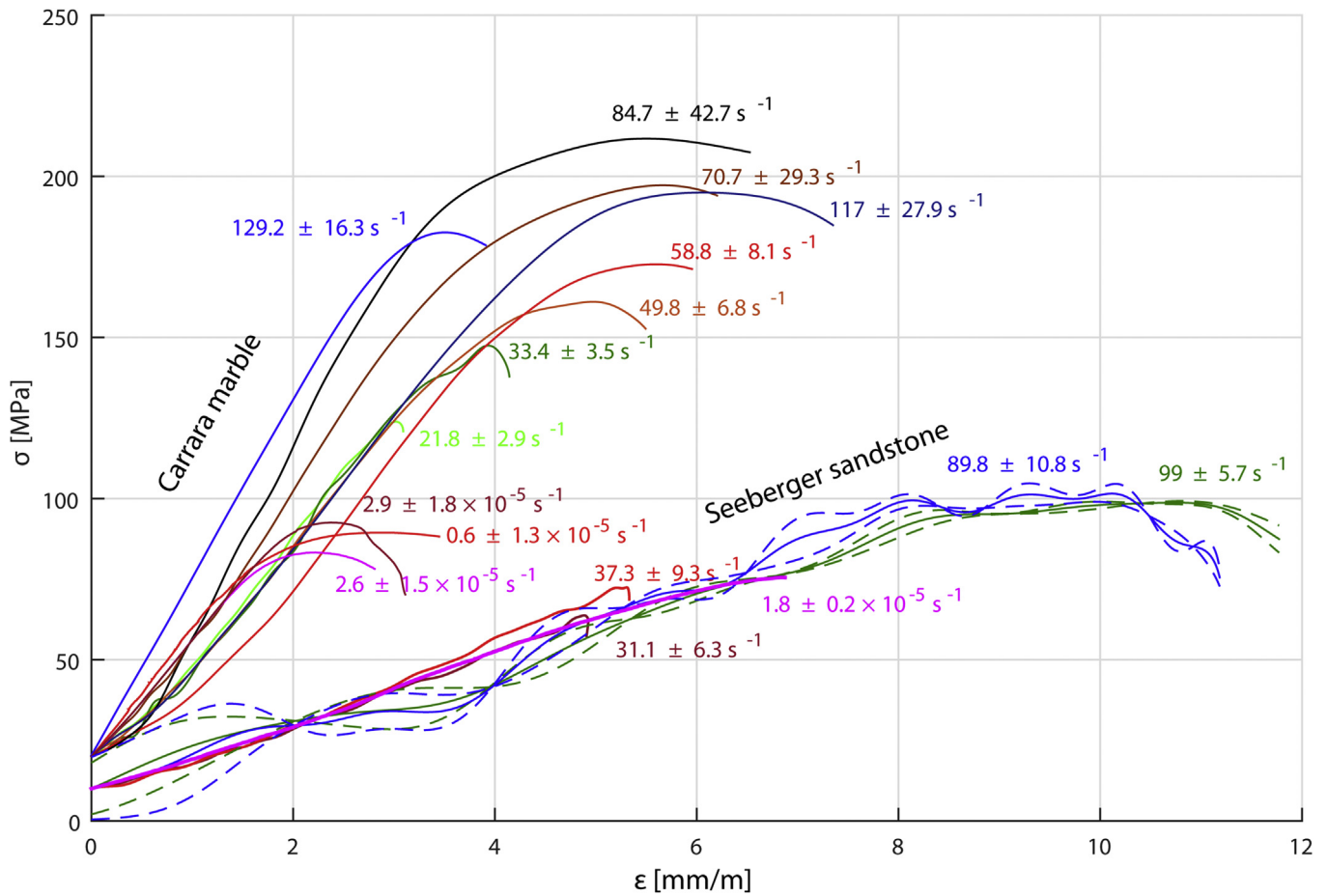
Fig. 6. Stress-strain response of Seeberger sandstone and Carrara marble at various rates of deformation. Experiments with insufficient stress equilibrium are represented by pairs of dashed lines with their average as a solid line. A significant increase in the linear stress-strain response can be observed at high strain rates for both rock types in comparison to quasi-statically deformed samples at rates of ~10^{-5} s^{-1}.

slightly greater than the initial tangent modulus (Jaeger et al., 2009). Nevertheless, increasing values of the marble's tangent modulus for high deformation rates occurs, indicating an even stronger increase in its actual Young's modulus. A least-squares-fitted linear function (Eq. (7)), as a function of the strain rate (appearing curved in the semi-logarithmic plot of Fig. 7), gives a

rough estimation of the expected dynamic elastic response E_d of Carrara marble at high strain rates of up to 10^{+2} s^{-1}, where

$$E_d = 41.8\ GPa + 74.7\ MPa \times \dot{\varepsilon}_E \tag{7}$$

although strong scattering of data points leads to a small coefficient of determination of $R^2 = 0.171$. Seeberger sandstone reveals no
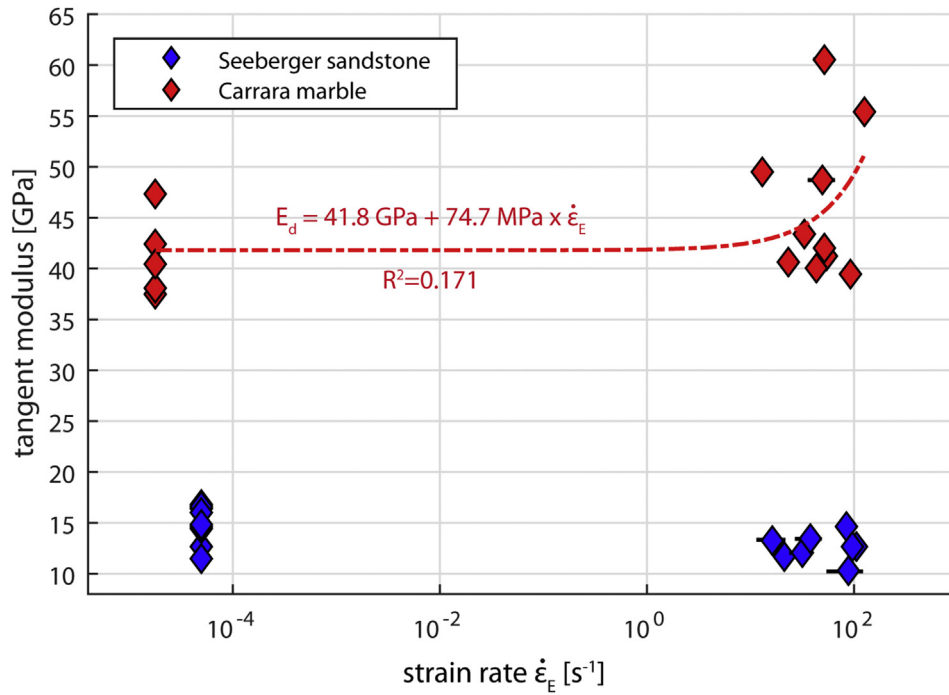
Fig. 7. Rate-dependent tangent modulus of Carrara marble and Seeberger sandstone and linear fit approximation of Carrara's dynamic Young's modulus E_d from quasi-static to high strain rates. Seeberger sandstone reveals no significant changes. Observed variances are expectable due to the natural variability of both materials.
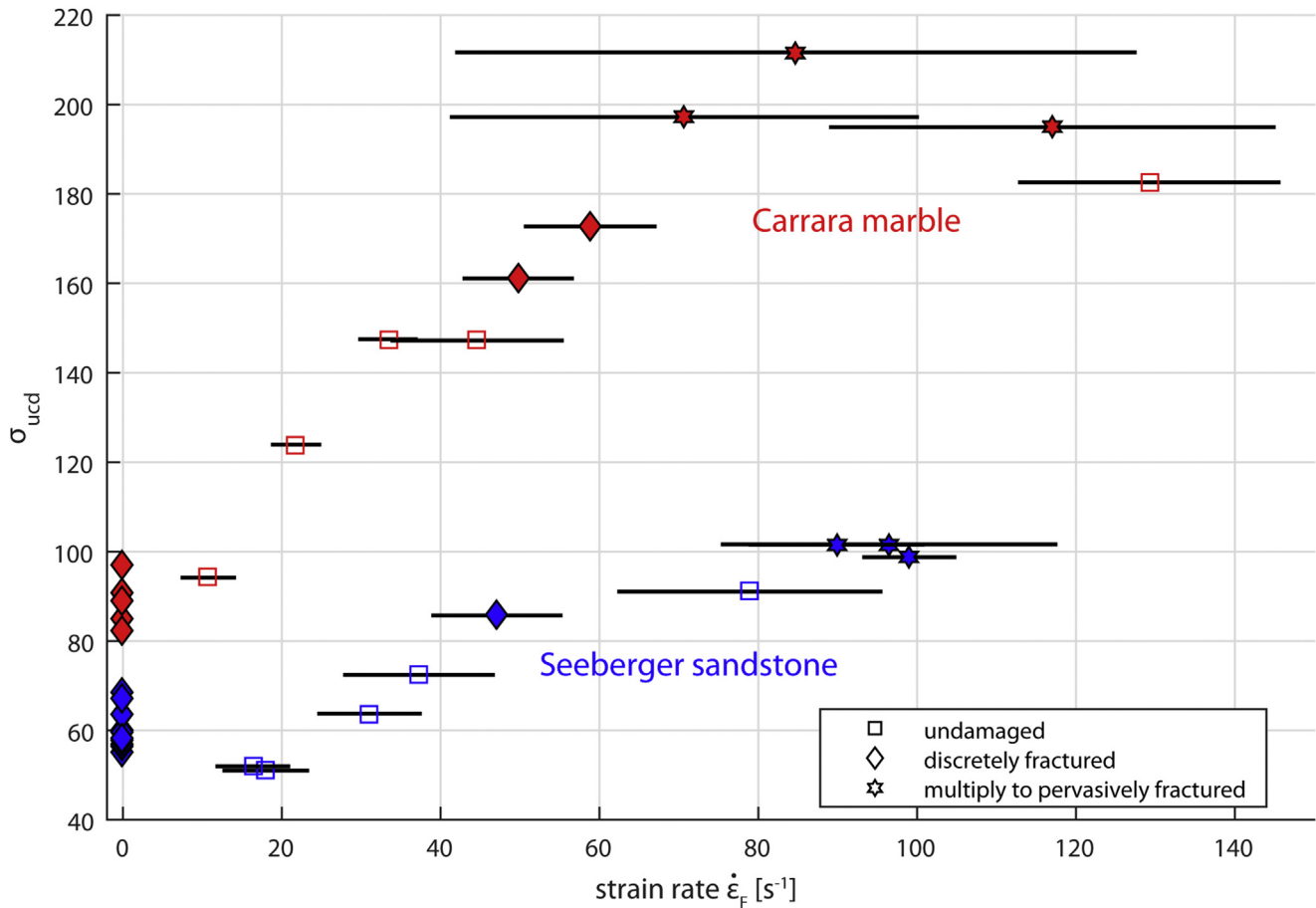

Fig. 8. Rate dependent (dynamic) uniaxial compressive strength σ_{ucd} as a function of the applied strain rate $\dot{\varepsilon}_F$ of Carrara marble and Seeberger sandstone, differentiating between unbroken, discretely and pervasively fractured samples. Horizontal error bars illustrate the variability of strain rate during individual tests.

significant changes at high strain rates, indicating a rather rate-insensitive elastic response.

On a linear scale, the dynamic uniaxial compressive strength σ_{ucd} of Seeberger sandstone and Carrara marble increase progressively as a function of the applied strain rate $\dot{\varepsilon}_F$ (Fig. 8). A typical semi-logarithmic representation of the same data normalized by quasi-static values σ_{ucs} as given in Table 1 illustrates the power law character of the dynamic strength enhancement. In Figs. 8 and 9, samples are categorized in terms of their post testing conditions. Macroscopically undamaged samples in this respect carry the information that the uniaxial compressive strength of the rock must be higher than the maximum applied stress at the given strain rate. Therefore, the approximated dashed trend lines of dynamic rock strength are above points of undamaged samples (Fig. 9). We also distinguished between pervasively failed samples and those that failed along a single or a few localized fractures to identify the transition to increasing pulverization of the specimens at higher strain rates. The trend lines are fitted to data points of broken samples on the basis of Eq. (8) (Kimberley et al., 2013):

$$\frac{\sigma_{ucd}}{\sigma_{ucs}} = 1 + \left(\frac{\dot{\varepsilon}}{\dot{\varepsilon}_0}\right)^{\frac{2}{3}} \qquad (8)$$

where σ_{ucd} represents the dynamic rock strength, and σ_{ucs} the respective quasi-static rock strength. $\dot{\varepsilon}_0$ equals a material-dependent characteristic strain rate used as a normalizing factor, representing a theoretical function of the materials' elastic properties, initial flaw distribution and length, their interaction and fracture toughness. It was determined to be 170 s^{-1} for Seeberger sandstone and 65 s^{-1} for Carrara marble by fitting function to the data points. According to Kimberley et al. (2013) the compressive strength of a rock remains nearly constant below a transition strain rate of approximately $0.1 \times \dot{\varepsilon}_0$, while a rapid increase is expected beyond that transition. The ratio of σ_{ucd} to σ_{ucs} at a given strain rate (commonly at 100 s^{-1}) is known as the dynamic increase factor ($DIF = \frac{\sigma_{ucd}}{\sigma_{ucs}}$). Results point to an earlier onset of dynamic behavior of the carbonate rock with a DIF of about 2.2—2.4 at deformation rates of 100 s^{-1}, whereas the sandstone reveals a DIF of 1.6—1.7 at comparable strain rates.

4. Discussion

The present paper compares stress-strain and uni-axial compressive strength behavior of two very different rock types, tested at high strain rates. Seeberger sandstone is a fine-grained, highly porous, quartz-dominated rock, which depicts no significant strain rate sensitivity in its tangent modulus, confirming that a radial confinement due to strain acceleration has no significant influences at strain rates of 100 s^{-1}. However its uni-axial compressive strength experiences a dynamic increase of about 1.7 times of the quasi-static strength at these strain rates. Carrara marble is a non-porous, fine-grained carbonate rock that shows an earlier onset of the dynamic behavior, including a rate-dependent tangent modulus. This observation is in contradiction to results by Doan and Billi (2011), who reported a rate-independent Young's modulus of 10—20 GPa for Carrara marble at strain rates of up to 209 s^{-1}. However, they did not specify if pulse shaping techniques were used, since conventional cylindrical strikers produce rectangular incident pulses, where insufficient stress equilibrium leads to an overestimation of strain during the early experimental phase, prohibiting precise measurements of the Young's modulus.

The dynamic increase factor DIF shows a high variability based on this work and prior studies (Fig. 10). Comparing results of experimental studies from different authors is challenging, since
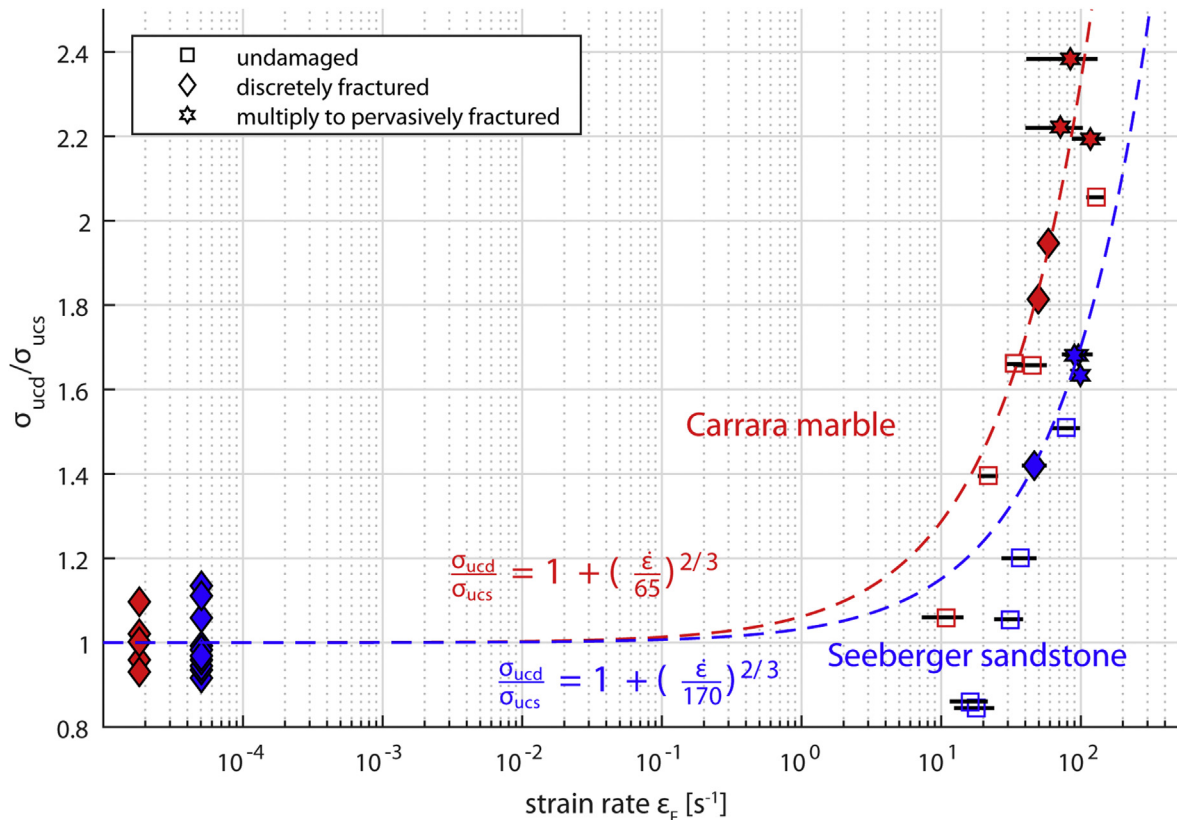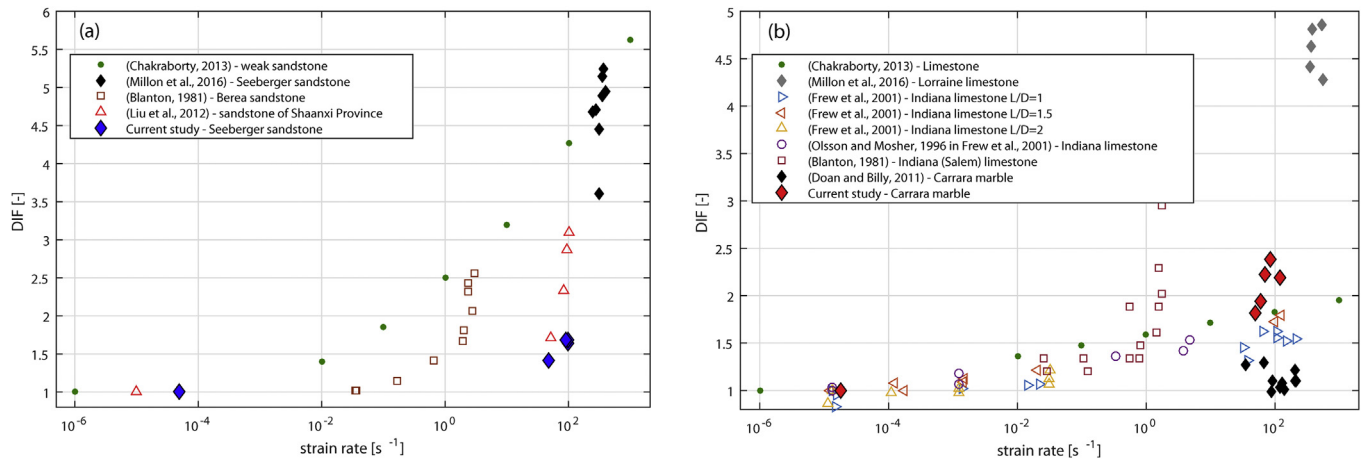

Fig. 9. Normalized rate dependent uniaxial compressive strength and functions describing the strength enhancement of Carrara marble and Seeberger sandstone at dynamic loading conditions. Error bars show that the variations of strain rate are within the magnitude of the representative strain rate.

Fig. 10. Comparison of current study results and literature data for different sandstones (a) and carbonate rocks (b). Frew et al. (2001) conducted experiments on samples of various length to diameter ratios (L/D) to investigate the effects of sample size.

Table 3
Summary of textural, compositional and experimental information given in literature data.

source	type/name/location	grain size [mm]	Porosity [%]	static compressive strength [MPa]	sample length; diameter [mm]	comments
Chakraborty (2013)	sandstone	–	–	–	12.7; 12.7	numerical simulation of weak sandstone behavior
Millon et al. (2016)	Seeberger sandstone	Ø 0.1	25	42.3 ± 2.4	[a]50; 60 [b]20; 75	–
Blanton (1981)	Berea sandstone	medium	19.1 ± 0.5	46 ± 4	50; 16.5	average strain rate given as representative rate
Liu et al. (2012)	Sandstone from Shaanxi Province	–	–	61.40	43; 97	high calcite content
Chakraborty (2013)	Limestone	–	–	–	12.7; 12.7	numerical simulation
Millon et al. (2016)	Limestone mined in Lorraine	–	31	9.8 ± 1.5	[a]50; 60 [b]20; 75	–
Frew et al. (2001)	Indiana limestone	0.15–1.0	15	–	12.7–25.4; 12.7	90% calcite, < 10% quartz
Frew et al. (2001)	Indiana limestone	0.15–1.0	15	–	50.8; 25.4	90% calcite, <10% quartz
Blanton (1981)	Indiana (Salem) Limestone	medium	12.5 ± 0.6	44 ± 9	50; 16.5	bioclastic
Doan and Billi (2011)	Carrara marble	0.2–0.4	–	about 100	27.65–28.75; 25.58–25.97	maximum strain rate given as representative rate

[a] Low-medium strain rates (20–83.3 s^{-1}).
[b] High strain rates (>275 s^{-1}).

(i) either the sample dimensions or microstructural rock characteristics vary, are not described at all, or (ii) the evaluation procedures are not consistent leading to systematic differences (Table 3).

4.1. A comparison with previous work on Seeberger sandstone and Carrara marble

Millon et al. (2016) conducted experiments on samples of Seeberger sandstone from the same quarry as the current study. However, in this quarry the succession of sandstone beds display some variations in grain size and porosity. They tested slightly larger samples of smaller length to diameter ratio (Table 3) at strain rates of 250–400 s^{-1}. Their results therefore complement the current study, since all data points appear along a typical power law function. Doan and Billi (2011) conducted SHPB tests on Carrara marble to investigate damage patterns of samples loaded at high strain rates. Their experimental results show maximum strain rate and maximum stress measured during individual experiments, using 100 MPa as the quasi-static normalizing factor. Therefore, we suppose a systematic overestimation of the strain rate in their data which indicates the importance of a consistent evaluation method

to determine the DIF. The use of the maximum strain rate as a representative value leads to a systematic overestimation in conventional SHPB tests.

4.2. Comparison with other lithologies

Including dynamic mechanical data of sandstones and limestones from other locations cause a larger scatter and spread of data owing to variations in petrography and specifications on sample characteristics (Fig. 10, Table 3). Small differences in microstructural properties, e.g., grain size, porosity and binding agent between rocks of the same type may have large influences on the dynamic behavior and are commonly neglected in high strain rate studies on rocks. Especially the composition and the amount of cementation, inversely associated with porosity, have major influence on the bulk rock mechanical behavior. For instance, Liu et al. (2012) investigated sandstones of comparably high calcite content, indicating a carbonate cementation, whereas Seeberger sandstone is weakly bonded by silicate. The length to diameter ratio of the sample L/D as investigated by Frew et al. (2001) may also influence the results as well as sample size (Table 3).

We observed an increase of the marble's tangent modulus, which raises the question about whether the loading phase at quasi-static rates of deformation has purely linear elastic behavior or is co-determined by secondary processes, reducing its linear stress-strain response in comparison to its high strain rate response. An early onset of micro-fracturing, the activation of cleavage plains or twinning at pressures far below yield strength are possible processes that could reduce its stiffness at quasi-static strain rates. The weakening mechanism may be inhibited at higher strain rates and may lead to a stiffer rock response. Kimberley et al. (2013) provide explanations for brittle failure mechanisms that lead to the observed dynamic increase in rock strength. Prior to failure, the most severe crack is initiated once the static yield stress is exceeded. This change causes a flattening of the stress-strain curves for both investigated rocks by progressive weakening of the material at quasi-static conditions (Fig. 6). This process seems to be inhibited at higherer strain rates, where the linear response proceeds far beyond that point for Seeberger sandstone and Carrara marble. The extension of the linear stress-strain response may be explained by a delocalization of the strain into a multitude of cracks as opposed to single fracturing, thereby removing increasing amounts of elastic energy and generating fracture surfaces at high strain rates. Post-mortem analysis of samples supports this hypothesis: the samples exhibit dozens of parallel cracks in longitudinal sample direction and a large amount of pulverized material, whereas quasi-static tests usually generate 1—5 discrete fractures only. Despite the intense fragmentation at high strain rates, samples frequently exhibit a residual cohesion. Specimens can withstand a total strain of about 0.6% for Carrara marble and 1.2% for Seeberger sandstone.

5. Conclusion

The split Hopkinson pressure bar (SHPB) technology represents an important method for investigating rocks experiencing fast strain rates. It is still a somewhat uncommon experimental method in structural geology, although an increasing number of reports document that seismogenic faulting occurs in this strain rate regime. This paper is intended to introduce the SHPB technique and presents the dynamic mechanical response under uniaxial compressive loading of two rocks, sandstone and marble. The onset of the dynamic behavior of marble precedes that of sandstone and the dynamic increase factor (DIF) of the uniaxial compressive strength for marble is about 2.2—2.4 at deformation rates of 100 s^{-1}, whereas the sandstone reveals a DIF of 1.6—1.7 at comparable strain rates. Although standards for dynamic testing have been developed by the International Society for Rock Mechanics ISRM (e.g., Zhou et al., 2012), it is still a challenging method because dispersion generates high frequency oscillations in incident stress pulses that cannot completely be eliminated. We utilized a modified method to determine representative strain rates assigned to linear elastic stress-strain response and brittle sample failure. If the Young's modulus cannot be measured precisely in SHPB tests due to unsatisfied stress equilibrium during the initial loading phase, a rough estimation can be done by comparison of both sample facet stresses σ_a, σ_b and the three-waves evaluation method (see Figs. 4 and 5). The dynamic strain rate-dependent behavior of geo-materials has significance for a broad spectrum of geological questions, in particular for the understanding of geohazards that are associated with fast deformation such as meteorite impact and earthquakes. Understanding the mechanical response and fragmentation behavior of rocks at fast strain rates will allow structural geologists to narrow down the conditions during large-scale seismic movements on active and inactive faults.

References

Blanton, T.L., 1981. Effect of strain rates from 10-2 to 10 sec-1 in triaxial compression tests on three rocks. Int. J. Rock Mech. Min. Sci. Geomech. Abstr. 18, 47—62. http://dx.doi.org/10.1016/0148-9062(81)90265-5.

Bouchon, M., Vallée, M., 2003. Observation of long supershear rupture during the magnitude 8.1 Kunlunshan earthquake. Science 301, 824—826.

Buhl, E., Kowitz, A., Elbeshausen, D., Sommer, F., Dresen, G., Poelchau, M.H., Reimold, W.U., Schmitt, R.T., Kenkmann, T., 2013. Particle size distribution and strain rate attenuation in hypervelocity impact and shock recovery experiments. J. Struct. Geol. 56, 20—33. http://dx.doi.org/10.1016/j.jsg.2013.08.007.

Chakraborty, T., 2013. Impact simulation of rocks under SHPB test. Proc. Indian Natl. Sci. Acad. 79, 605—613. http://dx.doi.org/10.16943/ptinsa/2013/v79i4/47985.

Chen, W.W., Song, B., 2010. Split Hopkinson (Kolsky) Bar: Design, Testing and Applications. Mechanical Engineering Series. Springer, New York, Dordrecht, Heidelberg, London, p. 388.

Christensen, R.J., Swanson, S.R., Brown, W.S., 1972. Split-Hopkinson-bar tests on rock under confining pressure. Exp. Mech. 12 (11), 508—513. http://dx.doi.org/10.1007/BF02320747.

Collins, G.S., Melosh, H.J., Marcus, R.A., 2005. Earth Impact Effects Program: a Web-based computer program for calculating the regional environmental consequences of a meteoroid impact on earth. Meteorit. Planet. Sci. 40 (6), 817—840. http://dx.doi.org/10.1111/j.1945-5100.2005.tb00157.x.

Davies, T.R., McSaveney, M.J., 2009. The role of rock fragmentation in the motion of large landslides. Eng. Geol. 109, 67—79. http://dx.doi.org/10.1016/j.enggeo.2008.11.004.

Di Toro, G., Han, R., Hirose, T., De Paola, N., Nielsen, S., Mizoguchi, K., Ferri, F., Cocco, M., Shimamoto, T., 2011. Fault lubrication during earthquakes. Nature 471, 494—498. http://dx.doi.org/10.1038/nature09838.

Doan, M.L., Billi, A., 2011. High strain rate damage of Carrara marble. Geophys. Res. Lett. 38, 19. http://dx.doi.org/10.1029/2011GL049169.

Doan, M.L., Gary, G., 2009. Rock pulverization at high strain rate near the San Andreas fault. Nat. Geosci. 2 (10), 709—712. http://dx.doi.org/10.1038/ngeo640.

Ebert, M., Hecht, L., Deutsch, A., Kenkmann, T., 2013. Chemical modification of projectile residues and target material in a MEMIN cratering experiment. Meteorit. Planet. Sci. 48 (1), 134—149. http://dx.doi.org/10.1111/j.1945-5100.2012.1429.x.

Fondriest, M., Aretusini, S., Di Toro, G., Smith, S.A., 2015. Fracturing and rock pulverization along an exhumed seismogenic fault zone in dolostones: the Foiana Fault Zone (Southern Alps, Italy). Tectonophysics 654, 56—74. http://dx.doi.org/10.1016/j.tecto.2015.04.015.

Frew, D.J., Forrestal, M.J., Chen, W., 2001. A split Hopkinson pressure bar technique to determine compressive stress-strain data for rock materials. Exp. Mech. 41 (1), 40—46. http://dx.doi.org/10.1007/BF02323102.

Frew, D.J., Forrestal, M.J., Chen, W., 2002. Pulse shaping techniques for testing brittle materials with a split Hopkinson pressure bar. Exp. Mech. 42 (1), 93—106. http://dx.doi.org/10.1007/BF02411056.

Grady, D.E., Kipp, M.E., 1993. Dynamic fracture and fragmentation. In: Asay, J.R., Shahin-poor, M. (Eds.), High-pressure Shock Compression of Solids. Springer, New York, pp. 265—322.

Gray, G.T., 2000. Classic Split-hopkinson Pressure Bar Testing. ASM Handbook, Mechanical Testing and Evaluation, vol. 8. ASM International, Materials Park OH, pp. 462—476.

Hakalehto, K.O., 1970. Brittle fracture of rocks under impulse loads. Int. J. Fract. Mech. 6 (3), 249—256. http://dx.doi.org/10.1007/BF00212655.

Heaton, T.H., 1990. Evidence for and implications of self-healing pulses of slip in earthquake rupture. Phys. Earth Planet. Inter. 64, 1—20.

Hild, F., Forquin, P., Cordeiro da Silva, A.R., 2003. Single and multiple fragmentation of brittle geomaterials. Rev. francaise génie Civ. 7 (7—8), 973—1002. http://dx.doi.org/10.1080/12795119.2003.9692529.

Hong, L., Zhou, Z.L., Yin, T.B., Liao, G.Y., Ye, Z.Y., 2009. Energy consumption in rock fragmentation at intermediate strain rate. J. Central South Univ. Technol. 16, 677—682. http://dx.doi.org/10.1007/s11771-009-0112-5.

Jaeger, J.C., Cook, N.G., Zimmerman, R., 2009. Fundamentals of Rock Mechanics. John Wiley & Sons.

Kenkmann, T., Poelchau, M.H., Wulf, G., 2014. Invited review: structural geology of impact craters. J. Struct. Geol. 62, 156—182. http://dx.doi.org/10.1016/

j.jsg.2014.01.015.

Kimberley, J., Ramesh, K.T., Daphalapurkar, N.P., 2013. A scaling law for the dynamic strength of brittle solids. Acta Mater. 61 (9), 3509–3521. http://dx.doi.org/10.1016/j.actamat.2013.02.045.

Li, X.B., Lai, H.H., Gu, D.S., 1993. Energy absorption of rock fragmentation under impulsive loads with different wave forms. Trans. Nonferr. Metal. Soc. 3 (1), 1–5.

Liu, J.Z., Xu, J.Y., Lv, X.C., Zhao, D.H., Leng, B.L., 2012. Experimental study on dynamic mechanical properties of amphibolites, sericite-quartz schist and sandstone under impact loadings. Int. J. Nonlinear Sci. Numer. Simul. 13 (2), 209–217. http://dx.doi.org/10.1515/ijnsns-2011-121.

Melosh, H.J., 1989. Impact Cratering: a Geologic Process. Oxford Univ. Press, New York.

Millon, O., Ruiz-Ripoll, M.L., Hoerth, T., 2016. Analysis of the behavior of sedimentary rocks under impact loading. Rock Mech. Rock Eng. http://dx.doi.org/10.1007/s00603-016-1010-4.

Mohr, D., Gary, G., Lundberg, B., 2010. Evaluation of stress-strain curve estimates in dynamic experiments. Int. J. Impact Eng. 37 (2), 161–169. http://dx.doi.org/10.1016/j.ijimpeng.2009.09.007.

O'Keefe, J.D., Ahrens, T.J., 1975. Shock effects from a large impact on the moon. Lunar Planet. Sci. Conf. Proc. 6, 2831–2844.

Passelègue, F.X., Schubnel, A., Nielsen, S., Bhat, H.S., Madariaga, R., 2013. From sub-Rayleigh to supershear ruptures during stick-slip experiments on crustal rocks. Science 340, 1208–12011.

Pieri, M., Burlini, L., Kunze, K., Stretton, I., Olgaard, D.L., 2001. Rheological and microstructural evolution of Carrara marble with high shear strain: results from high temperature torsion experiments. J. Struct. Geol. 23 (9), 1393–1413. http://dx.doi.org/10.1016/S0191-8141(01)00006-2.

Poelchau, M.H., Kenkmann, T., Thoma, K., Hoerth, T., Dufresne, A., Schäfer, F., 2013. The MEMIN research unit: scaling impact cratering experiments in porous sandstones. Meteorit. Planet. Sci. 48, 8–22. http://dx.doi.org/10.1111/maps.12016.

Poelchau, M.H., Michalski, C., Deutsch, A., Thoma, K., Schäfer, F., Kenkmann, T., 2015. Experimental cratering in Carrara marble: latest results from the MEMIN research unit. In: Lunar and Planetary Science Conference, vol. 46, p. 2447.

Ramesh, K.T., Hogan, J.D., Kimberley, J., Stickle, A., 2015. A review of mechanisms and models for dynamic failure, strength, and fragmentation. Planet. Space Sci. 107, 10–23. http://dx.doi.org/10.1016/j.pss.2014.11.010.

Ravichandran, G., Subhash, G., 1994. Critical appraisal of limiting strain rates for compression testing of ceramics in a split Hopkinson pressure bar. J. Am. Ceram. Soc. 77 (1), 263–267. http://dx.doi.org/10.1111/j.1151-2916.1994.tb06987.x.

Reches, Z., Dewers, T.A., 2005. Gouge formation by dynamic pulverization during earthquake rupture. Earth Planet. Sci. Lett. 235 (1), 361–374. http://dx.doi.org/10.1016/j.epsl.2005.04.009.

Scholz, C.H., 2002. The Mechanics of Earthquakes and Faulting. Cambridge university press.

Schuler, H., 2004. Experimentelle und numerische Untersuchungen zur Schädigung von stoßbeanspruchtem Beton. PhD thesis. Universität der Bundeswehr München, Universitätsbibliothek.

Spray, J.G., 2010. Frictional melting processes in planetary materials: from hypervelocity impact to earthquakes. Annu. Rev. Earth Planet. Sci. 38, 221–254.

Yuan, F., Prakash, V., Tullis, T., 2011. Origin of pulverized rocks during earthquake fault rupture. J. Geophys. Res. Solid Earth 116 (B6), 1978–2012. http://dx.doi.org/10.1029/2010JB007721.

Zang, A., Wagner, F.C., Stanchits, S., Janssen, C., Dresen, G., 2000. Fracture process zone in granite. J. Geophys. Res. Solid Earth 105 (B10), 23651–23661, 23651–23661.

Zhang, M., Wu, H.J., Li, Q.M., Huang, F.L., 2009. Further investigation on the dynamic compressive strength enhancement of concrete-like materials based on split Hopkinson pressure bar tests. Part I: experiments. Int. J. impact Eng. 36 (12), 1327–1334. http://dx.doi.org/10.1016/j.ijimpeng.2009.04.009.

Zhang, Q.B., Zhao, J., 2014. A review of dynamic experimental techniques and mechanical behaviour of rock materials. Rock Mech. Rock Eng. 47 (4), 1411–1478. http://dx.doi.org/10.1007/s00603-013-0463-y.

Zhou, Y.X., Xia, K., Li, X.B., Li, H.B., Ma, G.W., Zhao, J., Zhou, Z.L., Dai, F., 2012. Suggested methods for determining the dynamic strength parameters and mode-I fracture toughness of rock materials. Int. J. Rock Mech. Min. Sci. 49, 105–112.